

1 Chapter 1

Figure 1: The PEM system layout at LLO during O3, as seen on the PEM public website.

Figure 2: Schematic of a simple Michelson interferometer designed for GW

2 Chapter 2

3 Chapter 3

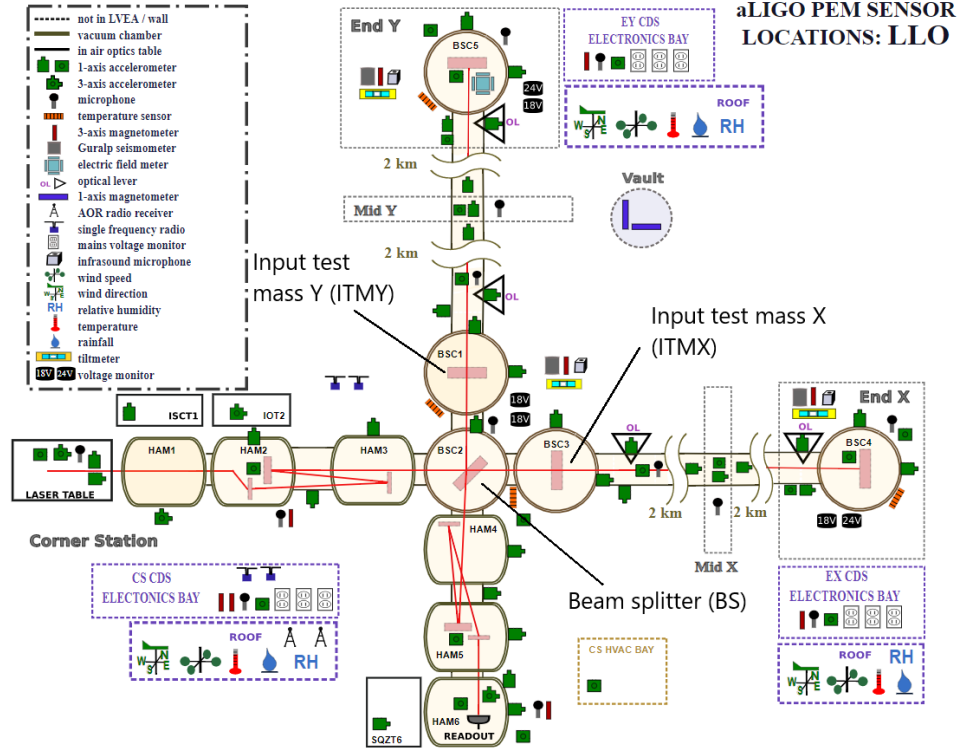


Figure 3: The PEM system layout at LLO during O3, as seen on the PEM public website.

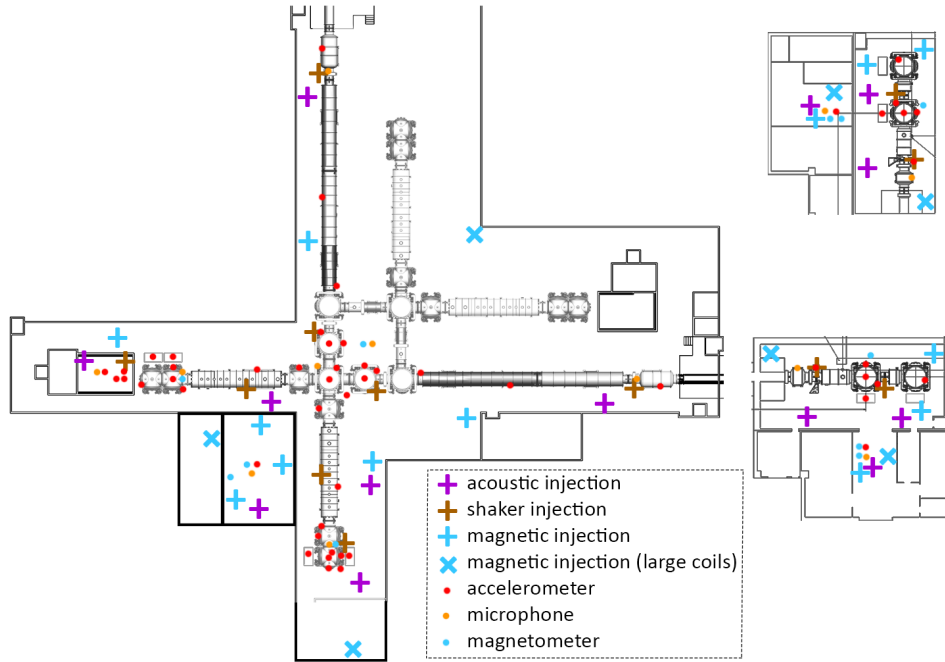


Figure 4: Standard locations for vibration and magnetic injections at the LHO corner station (left), Y end station (top right), and X end stations (bottom right).



Figure 5: Injection equipment photos. From left to right: wall-mounted magnetic field injection coil; 14-in. speakers; APS 113 shaker connected to the door of a vacuum chamber by a rigid fiberglass rod; modified Piezosystem shaker clamped to an electronics rack; modified B&K shaker clamped to a beam tube support.

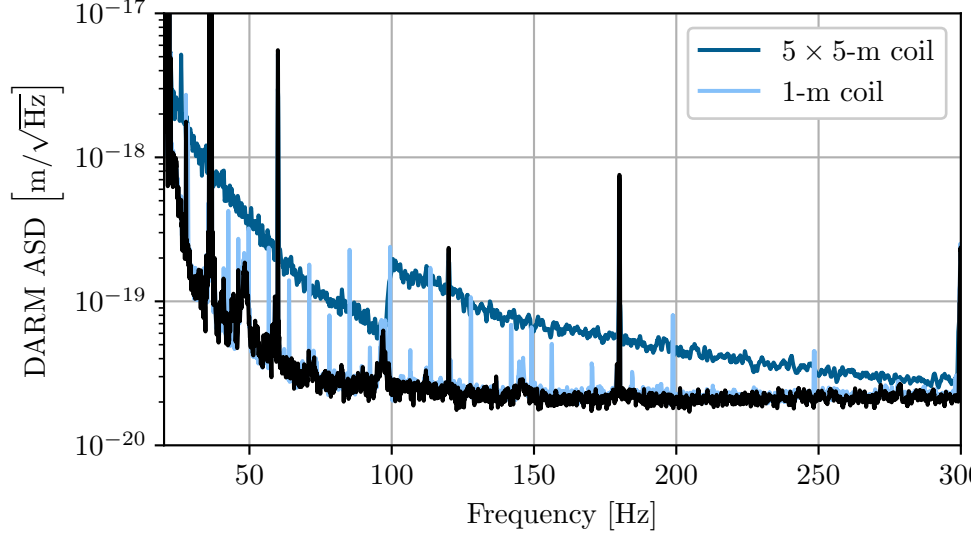


Figure 6: Comparison of the old small-coil comb magnetic field injections with the new large-coil broadband injections.

Figure 7: Illustration of an injection signal propagating to an auxiliary sensor and a coupling site. For distant injection sources, the small-angle approximation allows us to treat a sensor near a coupling site as a witness of the noise that couples into the interferometer.

Figure 8: Illustration of multiple subsequent injections, auxiliary sensors, and coupling sites.

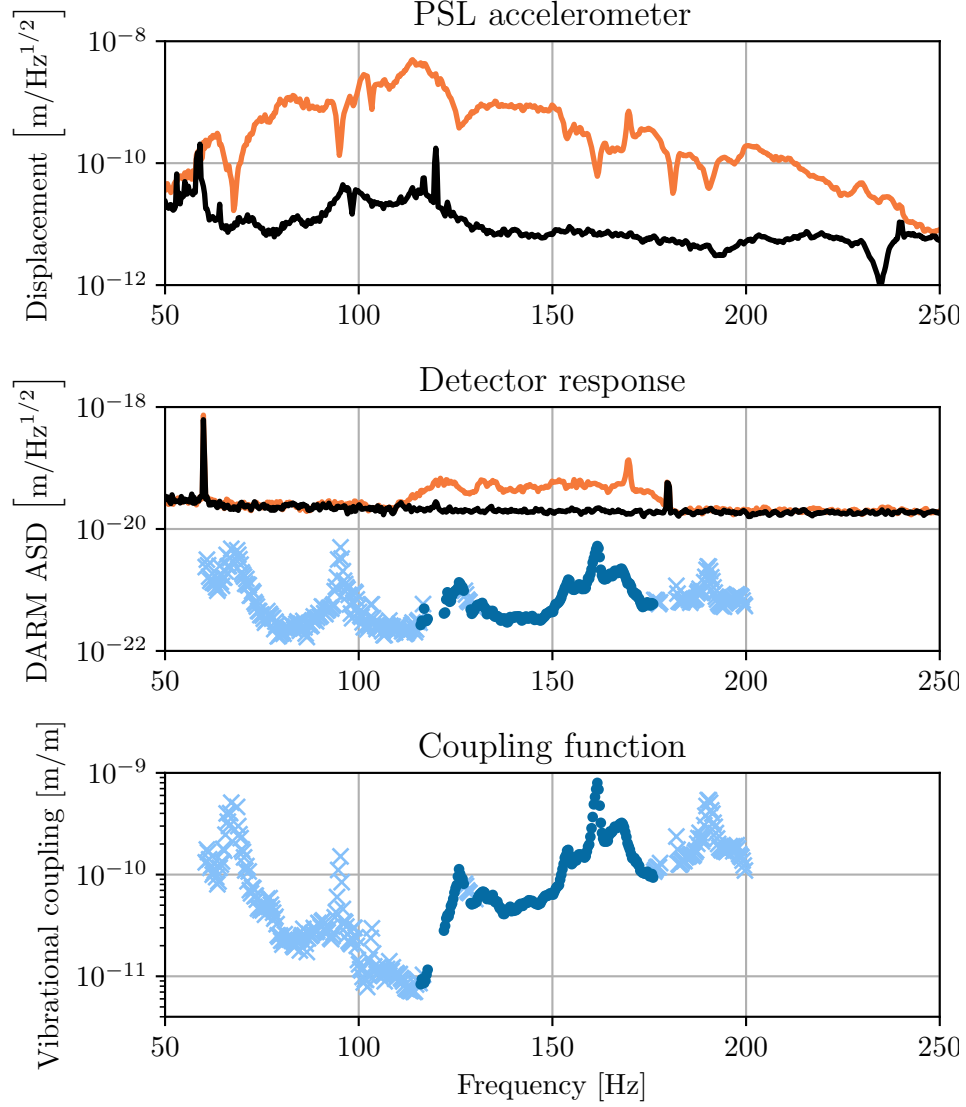


Figure 9: Example of a broadband acoustic noise injection and measurement of a single-injection coupling function. Top: displacement of an accelerometer in the PSL room during background time (black) and injection time (orange). Middle: DARM during background time (black) and injection time (orange). Estimated ambient levels for the accelerometer are shown as dark blue dots, with upper limits shown as light blue crosses. Bottom: single-injection coupling function used to produce estimated ambient above.

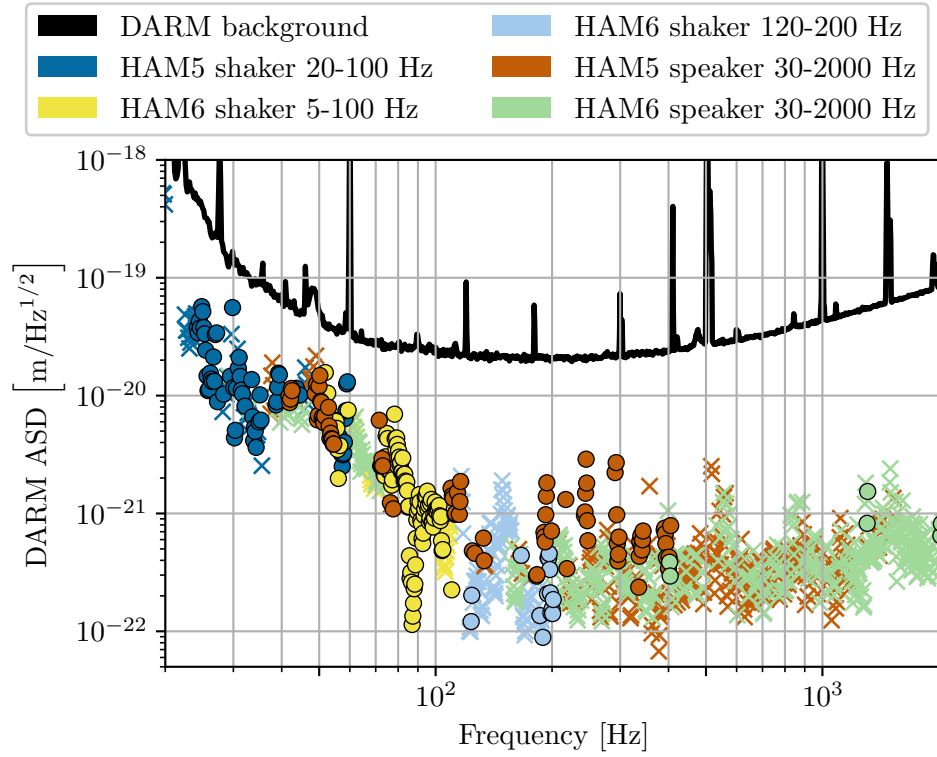


Figure 10: Ambient noise level for the LHO HAM6 Y-axis accelerometer estimated from a composite coupling function, using acoustic and seismic injections near the output arm.

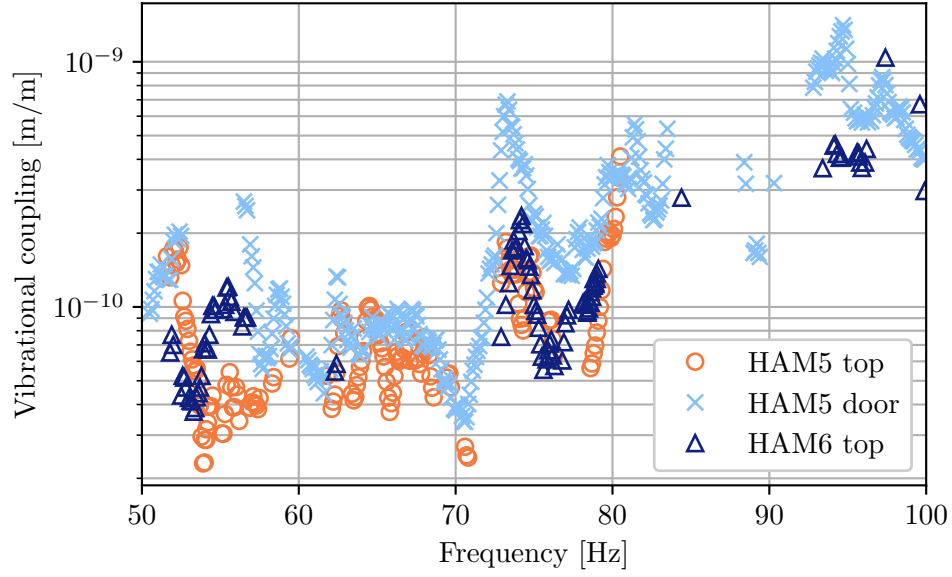


Figure 11: Single-injection coupling functions (upper limits not shown) for the HAM5 Y-axis accelerometer for three different shaker injection locations (on top of HAM5, on top of HAM6, and on the HAM5 chamber door).

Figure 12: Single-injection coupling functions (upper limits not shown) for various magnetometers and various injections at both observatories.

Figure 13: Applying spectral smoothing to the injection signal recorded by a microphone. Smoothing eliminates physical artifacts from the acoustic injection technique, recovering the expected broadband input signal.

4 Chapter 4

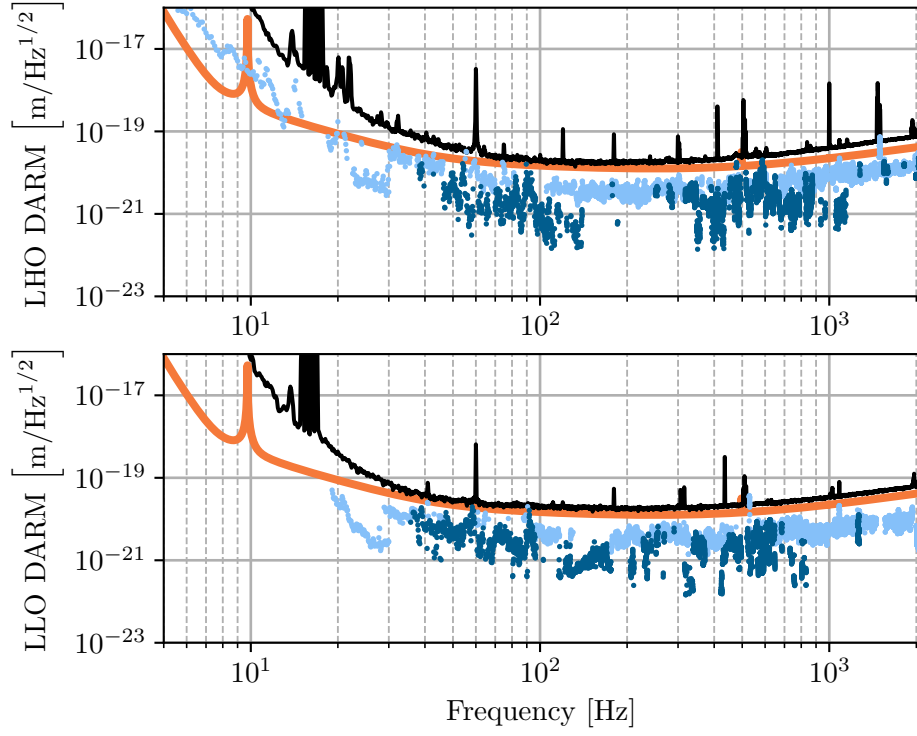


Figure 14: Ambient estimate of vibrational noise levels at LHO (top) and LLO (bottom).

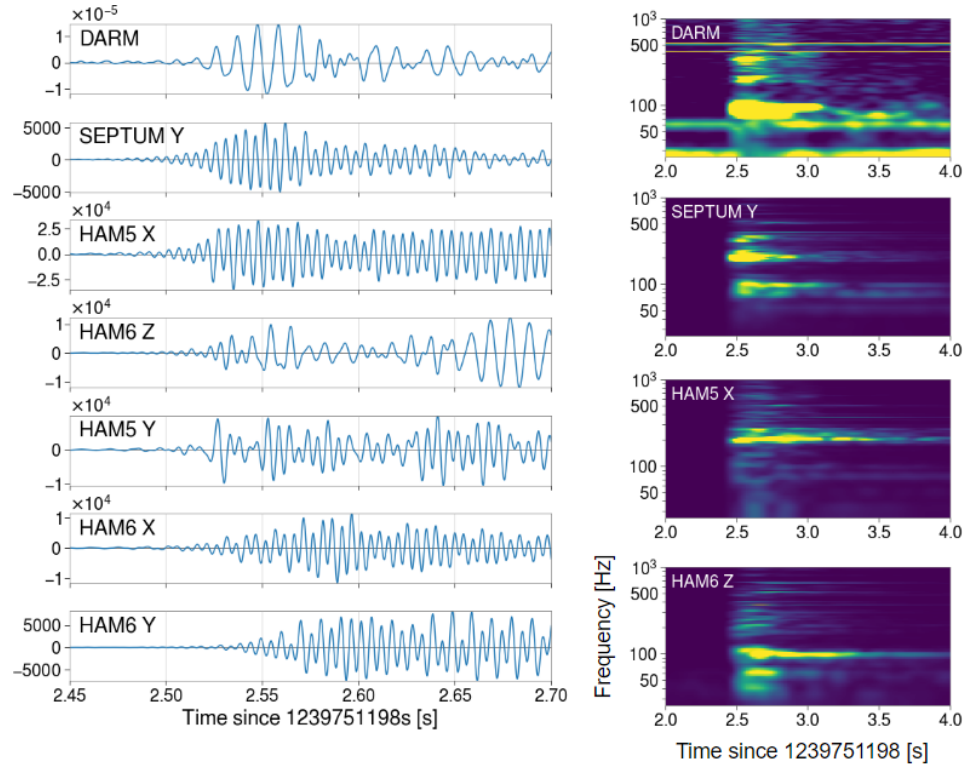


Figure 15: Time series (left) and spectrograms (right) of a vibrational impulse injection produced at the output arm of the LHO detector.

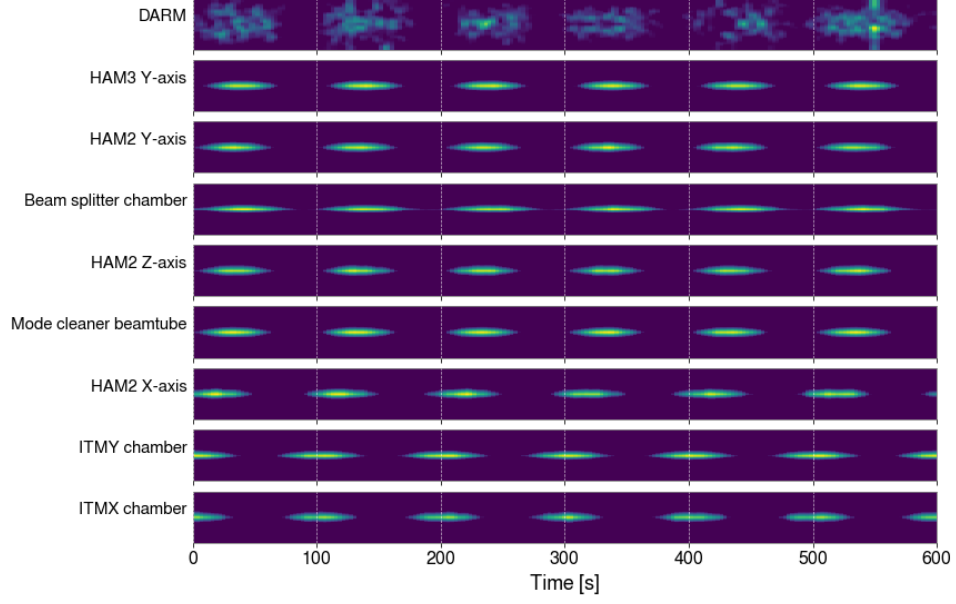


Figure 16: Spectrograms of DARM and various accelerometers near the input arm and beam splitter showing a beating-shakers injection at 48 Hz.

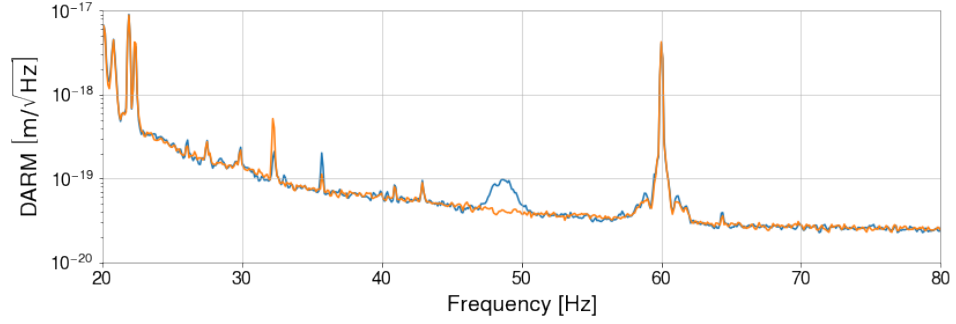


Figure 17: LHO DARM spectrum before and after mitigation of the 48-Hz peak.

Figure 18: Improvement in jitter coupling at LHO (left) and LLO (right) between the start and end of O3.

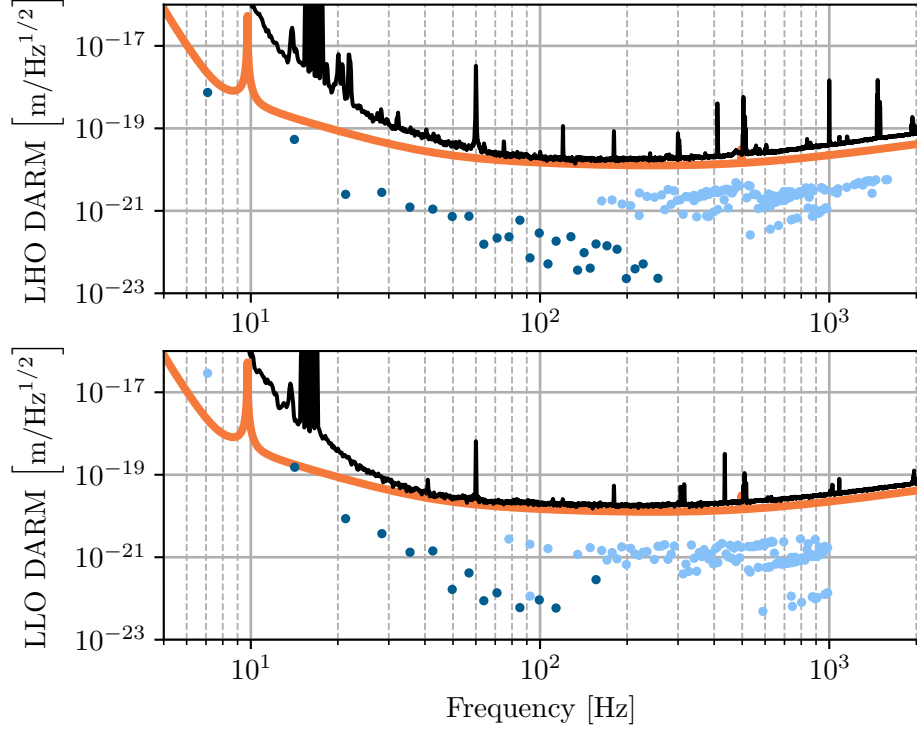


Figure 19: Ambient estimate of magnetic noise levels at LHO during March 2019 (blue), prior to O3, and during April 2019 (orange), after O3.

Figure 20: Ambient estimate of magnetic noise levels at LHO during March 2019 (blue), prior to O3, and during April 2019 (orange), after O3.

Figure 21: Weekly trends in frequency (top) and amplitude (top) of peaks in the magnetic coupling functions.

Figure 22: Constant-Q spectrogram of GW170817.

Figure 23: Constant-Q spectrogram of an accelerometer on the PSL table (top) and ambient magnetic noise levels for the same magnetometer (bottom).

Figure 24: Constant-Q spectrogram of an accelerometer on the LLO ETMY chamber (top) and ambient magnetic noise levels for the same accelerometer (bottom).

5 Chapter 5